Analysis of natural rock slope deformations under temperature variation: A case from a cool temperate region in Japan

Azania Mufundirwa[a, *], Yoshiaki Fujii[b, 1], Nariaki Kodama[c], and Jun-ichi Kodama[b]
[a] Graduate School of Engineering, Hokkaido University, N13W8, Sapporo, 060-8628, Japan
[b] Faculty of Engineering, Hokkaido University, N13W8, Sapporo, 060-8628, Japan
[c] Hakodate National College of Technology, Hakodate, 042-8501, Japan
([*]Corresponding author E-mail: azania.mufundirwa@eng.hokudai.ac.jp, Fax: + 81 11 706 6299)
[1] E-mail: fujii6299@eng.hokudai.ac.jp (Y. Fujii)

ABSTRACT

In this paper, natural rock slope deformation across fractures predominantly in a chert rock mass was monitored using six surface fracture displacement sensors, and the deformations arising from thermal stresses were predicted using (5 m × 5 m) two-dimensional (2-D) finite element (FE) plane strain analysis coupled with a model for rock mass expansion due to freezing of pore water. A new and simple method to minimize displacement proportional to temperature (due to thermal response of chert rock mass and sensor) was proposed. By applying the method, the corrected displacement, u', can be well recognized. Under u', clear rock mass movement, which could be related to fracture growth was observed. In addition, progressive fracture opening and closure was noted. Results from this study indicate insignificant influences of weather conditions on fracture/rock mass movement. Furthermore, under numerical analysis (FE), in the rock mass model (with 1 m deep fracture), tensile stresses that were large enough to induce fracture growth appeared at the fracture tip when temperature lowered. And in the rock slope model (with 1 m deep fracture), small tensile stresses, which were sufficient to cause fracture growth along the planes of weakness were observed. This research suggests that freezing effects on deformation of chert rock mass are insignificant, and we tentatively suggest that thermal fatigue predominantly caused the permanent fracture deformations.

KEY WORDS: Natural rock slope; Fracture; Displacement; Freezing; Finite element (FE)

1. Introduction

In Japan, some fatal accidents have occurred in the past due to large-scale slope collapse onto roads and railways, disrupting transportation and normal daily activities (Saito, 1965, 1969; Shiotani, 2003). As a result, ensuring the stability of rock slopes is a major priority. Continuous in-situ monitoring is vital to assess slope stability during the service life (Corkum and Martin, 2004; Rose and Hungr, 2007; Stemberk et al., 2010). Various methods of assessing slope stability have been in practical use, e.g., rock mass classification systems (Nicholson et al., 2000a; Pantelidis, 2009). In a broad sense, numerous factors contribute to rock slope destabilization. Nicolson and Hencher (1997) discuss agents of rock slope deterioration, which include physical and chemical processes, e.g., stress release, cycles of wetting and drying, etc (Matsuoka, 2008). They suggested that these mechanisms could cause dilation of existing open and incipient discontinuities allowing ingress of water, rock fragments, organic material, and other damaging elements, hence destabilizing rock slopes. More importantly, the presence of fractures could also affect rock mass strength and increase ingress of water thereby causing instability (Alder and Thovert, 1999).

In cold regions, cycles of freezing and thawing could cause rock slope instabilities (Matsuoka, 2001, 2008; Nicholson and Nicholson, 2000b). Matsuoka (2001) reported two seasonal peaks of joint widening (sandstone) in autumn and spring. He concluded that, autumn events are associated with short-term freeze-thaw cycles, and that the magnitude of joint widening reflected freezing intensity and

water availability. On the other hand, he highlighted that the spring events were likely due to refreezing of meltwater entering the joint, thereby giving rise to the volumetric expansion/ ice expansion that possibly led to joint widening (Davidson and Nye, 1985). This may also explain the occurrence of rock falls in early spring, due to thawing of snow and frozen rocks, which may cause rock mass deterioration by stress corrosion at the crack tips (Ishikawa et al., 2004). In a study by Ishikawa et al. (2004), crack widths and rock temperatures were monitored on andestic bedrock in northern Japan (cold region). They found that a combination of liquid water infiltrating to the crack tip and subsequent freezing were the most significant contribution to brittle failure. Furthermore, they concluded that sub-critical crack movements correlated well with cyclic thermal stress at the crack tips. Murton et al. (2006) introduced the concept of rock fracture and crack growth by ice segregation in cold regions. In line with that, Matsuoka (2008), reinforces ice segregation as emanating from long-term slowing freezing. In addition, frost weathering in freezing porous media also results in rock fracturing and deterioration by ice lens growth and segregation (Akagawa and Kodama, 2005).

Thermal effects on rock mass deformation are also a practical concern. Ishiguro and Nakaya (1986) and Waragai (1998) mentioned that the possibility of crack/fracture initiation due to temperature variations must be taken into consideration for structural safety: temperature fluctuations in the rock mass could be caused by external weather conditions or by heat generation in the sub-surface environment.

From the discussion above, we have found that, mostly, no single thermal criterion can explain frost weathering (Matsuoka, 2001). Therefore, it is essential to understand fracture behaviour under various conditions, especially under temperature changes (Kostak et al., 1998).

In this paper, a 767-day long displacement and temperature record for a natural rock slope in Iwate prefecture (Shimohei district, Kawai village) in Japan is described (Fig. 1a). Fracture displacement sensors were installed on the surface of natural rock slope for continuous measurement of rock slope deformations. A new and simple method was proposed to reduce the apparent displacements (masking the true rock mass displacements) so that we could get more accurate displacements. The thermal behaviours of a rock mass and a rock slope, both with a one-metre deep fracture subjected to temperature variations were numerically analyzed (Reddy, 1993; Zienkiewicz and Taylor, 2005a; Zienkiewicz et al., 2005b). Important thermal deformation characteristics were deduced from the field measurements and numerical results.

2. Site and instrumentation

The study was conducted on a natural rock slope on a mountain-side in Iwate prefecture (Shimohei district, Kawai village) in Japan (Fig. 1a). The topography of the steep rock slope with a dip (> 65^{o}) is shown in Fig. 1a. Geologically, the rock slope consists of a chert block with a high thermal conductivity (K = 7.40 W/ m K, see Table 1), with some spatially distributed slates; both rocks are severely jointed within the North Kitakami Belt, the accretionary wedge. This area is located in the cool temperate zone.

Six surface fracture displacement sensors (ch1–ch6) were installed on the surface of natural rock slope as shown in Figs. 1b and 2. The fracture displacement sensors (Kyowa, BCD-5B model) had an operating range of −10 to 60 ^{o}C, a measuring range of ±5 mm, and a rated output of ±1 mV/V (2000×10^{-6}). Weather conditions namely, air temperature, humidity, snowfall, and rainfall were recorded from 9 November 2006 to present. Data till 14 December 2008 were analyzed (Fig. 1b). Data from all the instruments were recorded automatically at 30-minute intervals using a data logger (CR series, Campbell Scientific).

3. Characteristics of raw data

Variations of fracture displacement (u) and air

temperature (T_a) for the natural rock slope for each channel are shown in Fig. 3. Fundamentally, rock mass deforms with temperature variation. From observation, maximum and minimum temperatures achieved were 23 ^{o}C and –4.1 ^{o}C, respectively (ch1, Fig.3). Roughly, temperature-induced displacement varied sinusoidally with temperature, indicating thermal expansion/contraction (all channels, except ch2 in Fig. 3). This means other displacements that occur (e.g., sudden displacement trend changes), may be due to external factors/processes affecting fracture/rock mass movement (Nicolson and Hencher, 1997).

For ch1, in the range t = 257–286 days fracture/rock mass moved (ch1 in Fig. 3). It occurred during the summer period from 23 July 2007 to 21 August 2007. A sharp displacement of 0.2 mm was recorded. This displacement was not temperature-induced as illustrated with ch1 in Fig. 4. Furthermore, there was little rain 0–2.2 mm/day (see t = 257–286 days in Fig. 5a) and humidity was generally high (> 80%) as evidenced in Fig. 5b. Fracture displacement sensor, ch2, was installed on highly fractured rock mass (see ch2, Fig. 2). And, it gave variations of displacement significantly different from all the other channels (ch2 in Fig. 4). Ch2 has a positive slope, whilst the other channels have a negative slope (Fig. 4). The close linear relationship reflected in ch3 and ch5 (R^2 = 0.98 and 0.96), shows closeness to elastic (recoverable) deformations (Fig. 4). Ch4 and ch6 recorded some permanent deformations of 0.126 mm and 0.187 mm, respectively, from the start (**S**) to end (**E**) of monitoring (Fig. 4).

To some extent, the observed displacement data contain displacement components that are proportional to temperature caused by the thermal response of the rock mass, fracture displacement sensors and materials fixing/holding the sensors onto the surface of rock slope. Therefore, attempts to minimize these apparent displacement components were done in order to get the true displacement components due to external processes.

4. Corrected Displacements

4.1. Reduction of temperature bias on measured displacement

To minimize displacement components that are proportional to temperature, the following equations were used:

$$u' = u + AT_a \tag{1}$$

$$U_a = u'_{max} - u'_{min} \tag{2}$$

where u is measured displacement (one-day moving-average), u' is the corrected displacement, A is thermal correction coefficient, T_a is air temperature (one-day moving-average), U_a is displacement amplitude, u'_{max} is maximum corrected displacement, and u'_{min} is minimum corrected displacement.

First and foremost, different thermal correction coefficients, A, were determined for ch1–ch6. To compute A, "trial and error" was used, which is somewhat time consuming. Intuitively, the thermal correction coefficient, A, that gave the lowest/minimum displacement amplitude was used to correct the displacement (Fig. 6). In other words, a low A implies minimum temperature effects or erroneous displacements. With reference to Fig. 6, A ranges from +0.005 to +0.007 mm/^{o}C, except for ch2. For verification, the displacement sensor was calibrated in the laboratory and A = +0.00721 mm/^{o}C was obtained.

At ch2, A = –0.003 mm/^{o}C, which is different from other channels (Fig. 6). This may be attributed to the highly fractured nature of the surrounding rock mass within its vicinity (see ch2 in Fig. 2). Setup of the displacement sensor was different from the other channels as shown by the elongated bolt supporting the displacement sensor (ch2 in Fig. 2). This sensor arrangement might have impacted on the real/true rock displacement at ch2. Furthermore, at ch2, fracture tends to open or close with temperature variation

with some time lag (ch2 in Fig. 7).

Figure 7 shows that displacement variations at ch3 and ch5 are very small, and the possibility of fracture propagation is very low. At ch4, the fracture is gradually opening, and the possibility of fracture propagation is high (ch4 in Fig. 7). This phenomenon may be explained by creep or sub-critical fracture growth (inelastic fatigue) of the rock mass, because of the presence of cyclic thermal stresses at the crack tip (Ishikawa et al., 2004; Martin, 1972; Scholz, 1972). In contrast, at ch6 (Fig. 7), fracture is generally closing possibly due to viscous deformation.

Notably, relations between the corrected displacement and air temperature show near-horizontal patterns/slopes for ch3 and ch5 (Fig. 8); this indicates insignificant rock mass deformations. In principle, abnormal deviations from linearity are considered as fracture/rock mass movement caused by external processes, such as dilation of existing fractures by root growth, freeze-thaw and so forth (ch1 in Fig. 8). Small permanent deformations (0.0014–0.21mm) were observed in all the channels in two years (Fig. 8).

Essentially, after correction at ch1 in Fig. 7 (u' using A = +0.007 mm/^{o}C), the steep increase in fracture displacement (at $t \approx$ 36–40 weeks) became more apparent than in raw data (ch1 in Fig. 3). As an important feature, it was noted that the computed coefficients (+0.005 to +0.007 mm/^{o}C) are close to the determined laboratory coefficient (+0.00721 mm/^{o}C), except for ch2. This means that fractures in chert rock mass have little or insignificant deformations with temperature variation.

5. Using two-dimensional FE model

To get a better insight into the deformation of a fracture under temperature variation, numerical analyses for a rock mass with a one-metre deep fracture under temperature variations were carried out using (5 m × 5 m) two-dimensional plane strain analysis coupled with the fundamental heat transfer equation using the Crank-Nicolson method (Crank, 1975; William et al., 2007). Two boundary conditions were used; confined and unconfined conditions to simulate different in-situ conditions under elastic and elasto-plastic finite element analysis as shown in Fig. 9 (Timoshenko and Goodier, 1969). To simulate temperature in the field, two patterns of transient heat analysis (variable temperature boundary) were exclusively applied on the top rock surface under confined and unconfined conditions for a duration of 52 weeks. The first temperature pattern had a positive temperature variation (7.8–32.2 ^{o}C), with an initial rock mass temperature (T_{ref}) of 20 ^{o}C applied. The second temperature pattern had positive and sub-zero temperatures (−2.2–22.2 ^{o}C), with an initial temperature of 10 ^{o}C applied as the temperature of rock mass. With reference to Fig. 10, we defined:

$$\varepsilon_{f} = \alpha \, \Delta T \tag{3}$$

where ε_{f} is the accumulated thermal strain due to temperature variation, α is the thermal expansion coefficient of rock; ΔT is the change in temperature. It was assumed that rock expands from T_1 to T_2 due to freezing of pore water, where T_1 is the temperature at which freezing starts; T_2 is the temperature at which freezing ends (Fig. 10).

5.1. Analytical model

A two-dimensional finite element mesh was generated (864 triangular elements, 467 nodes). The thermal displacements in the x-direction under elastic analysis (u_x^{e}) and elasto-plastic analysis (u_x^{ep}) were calculated by considering nodal displacements of the fracture at the rock surface (node 442) as shown in Fig. 9. Stress in the x-direction (sigx/σ_x), normal to the fracture axis was mainly considered; it is these stresses that have a high possibility of causing fracture propagation. The model is symmetrical about the y-axis, and tensile stresses are taken as positive (+) whilst compressive stresses as negative (−) in these numerical analyses. Positive displacement means fracture

opening and negative displacement means fracture closure (Fig. 1c).

5.2. Analytic conditions

A total of 8 numerical simulations were performed; these are elastic and elasto-plastic analyses (confined and unconfined) under the two transient temperature patterns as mentioned above. For clarity, these are:

(1) Elastic model under confined boundary conditions;
(2) Elastic model under unconfined boundary conditions;
(3) Elasto-plastic model under confined boundary conditions; and
(4) Elasto-plastic model under unconfined boundary conditions.

The rock mass is assumed to be homogeneous and isotropic, and the properties of the rock mass used in the FE analyses are as in Table 1.

6. Numerical results and discussion

Thermal displacements under elastic (u_x^e) and elasto-plastic conditions (u_x^{ep}) were computed, and the stability of the natural rock mass was then assessed by analysing displacement from the numerical simulations.

6.1. Elastic analysis

Elastic-confined conditions under positive temperature (7.8–32.2 ^oC) were simulated as shown in Fig. 11. As temperature increased, the rock mass expanded, (e.g., at maximum temperature 32.2 ^oC, there is rock mass expansion) as shown in Fig. 11a. Initially, a slight aperture is assumed for the fracture so that the expansion is allowed. Expansion of rock mass across the fracture axis (Fig. 11a) practically means fracture closure as illustrated from t = 0–14 weeks in Fig. 12a. At the fracture tip, compressive stresses were observed, in which stress in the x-direction was less than the uniaxial compressive strength ($-\sigma_x < \sigma_c$); therefore no compressive failure was observed (Fig. 11b). As temperature decreased, the rock mass contracted (e.g., at minimum temperature 7.8 ^oC, rock mass contracted) as illustrated in Fig. 11c, thereby causing the fracture to open (see t = 26–39 weeks in Fig. 12a). Large tensile stresses around 30.8 MPa, in which stress in the x-direction was greater than the tensile strength of intact rock ($\sigma_x > \sigma_t$) were observed at the fracture tip (Fig. 11d). This condition could lead to fracture propagation, thereby deepening the fracture into the rock mass (Waragai, 1998). Displacement is almost linear with temperature (Fig. 12b). However, corrected displacement ($u_x'^e$) looks inelastic and irrecoverable although the model is completely elastic (Fig. 12d). This may be attributed to the slow heat transmission in the rock mass resulting in delayed deformations since our analysis commenced from an initial constant temperature of rock mass (e.g., 20 ^oC in the 7.8–32.2 ^oC range). In real world, the rock mass would have gone through many years/cycles of temperature variation since its formation.

Similarly, *elastic-unconfined* conditions within (7.8–32.2 ^oC) were analyzed. For brevity, it was also found that fracture tends to close and open with temperature increase and decrease, respectively. At minimum temperature of 7.8 ^oC, small tensile stresses of 13.2 MPa ($\sigma_x < \sigma_t$) appeared at fracture tip (Table 2); therefore fracture propagation is unlikely to occur.

For *elastic-confined* conditions within the –2.2 to 22.2 ^oC temperature range, (see Fig. 13), no compressive failure was observed (Fig. 13a). At minimum temperature –2.2 ^oC, large tensile stresses ($\sigma_x > \sigma_t$) were observed around the fracture tip (Fig. 13b). This condition could trigger fracture propagation. The maximum tensile stress generated (29.2 MPa) at –2.2 ^oC is smaller compared to that at minimum temperature of 7.8 ^oC (30.8 MPa), as shown in Table 2. This is due to expansion of rock mass as a result of freezing of pore water at sub-zero temperatures, which led to fracture closure, hence reducing tensile stresses around fracture tip (Murton et al., 2006). The expansion leading to fracture

closure (Davidson and Nye, 1985) is more apparent in the corrected displacement ($u_x^{'e}$), as illustrated by the dotted circle in Fig. 14c and d.

Notably, for *elastic-unconfined* conditions within the –2.2 to 22.2 °C temperature range, the lowest tensile stresses (12.4 MPa at –2.2 °C) were generated at fracture tip (Table 2). Because of unconfinement, tensile stresses tend to be distributed more broadly within the unconfined rock mass, rather than in confined conditions, hence the smaller tensile stresses generated at the fracture tip.

6.2. Elasto-plastic analysis

To understand the behaviour of chert rock mass, a different constitutive model (elasto-plastic) was used. Firstly, *elasto-plastic confined* conditions under a positive temperature range (7.8–32.2 °C) were conducted, and the results are shown in Fig 15a. Only confined conditions in which tensile stresses exceeded the tensile strength ($\sigma_x > \sigma_t$) are shown. For brevity, no element failures were observed in unconfined conditions (Table 3).

Remarkably, at minimum temperature 7.8 °C (Fig. 15a), there was tensile failure of 6 elements around the fracture tip. A small increase in fracture displacement (fracture propagation) is observed from t = 32–41 weeks as temperature decreased to a minimum level of 7.8 °C (Fig. 16a). Displacement gradually returned towards zero as temperature started to increase from t = 41–52 weeks (Fig. 16a).

Similarly, for *elasto-plastic confined* conditions (–2.2 to 22.2 °C, see Fig. 15b), at –2.2 °C, tensile failure of 4 elements occurred at the fracture tip (Fig. 15b). A small increase in displacement is observed from t = 33–44 weeks as temperature decreased to minimum levels in the zero-crossing range (Fig. 16b). Displacement gradually returned towards zero as temperature started to increase above 0 °C from t = 45–52 weeks (Fig. 16b).

7. Rock slope stability analysis

Having analyzed the rock mass model, we found it necessary to adopt a holistic rock slope model in order to get a better insight into the problem. Another two-dimensional rock slope model (FE) was proposed to simulate the field conditions of a steep vertical cliff as shown in Fig. 17. Elastic numerical analyses for the rock slope with a one-metre deep fracture, located at 0.25 m from a free steep rock surface, under temperature variation were carried out using a (5 m × 5 m) two-dimensional (plane strain) model (864 triangular elements, 475 nodes) as shown in Fig. 17. The same temperature variations were introduced in the rock slope model as mentioned in Section 5. Relative displacement at the fracture surface (nodes 451 and 452) was mainly considered to compute fracture displacement,

$$\Delta u_x = u_{x(452)} - u_{x(451)} \tag{4}$$

where Δu_x is the change in width of fracture in the x-direction, $u_{x(452)}$ is fracture displacement at node 452 in the x-direction and similarly, $u_{x(451)}$ is fracture displacement at node 451 in the x-direction.

7.1. Modelling results

For both temperature variations, similar phenomena of fracture closure with rock mass expansion and vice-versa was found as illustrated in Fig. 11a and c. Using the rock slope model (Fig. 17), *elastic* analysis under transient temperature range (7.8–32.2 °C) was conducted, and the results are as shown in Fig. 18. For example, at 7.9 °C, fracture opened although low tensile stresses (≈ 1.5 MPa) appeared at the fracture tip (Fig. 18b). This condition is sufficient to cause fracture growth by thermal fatigue along planes of weakness. Furthermore, tensile stresses ≈ 9 MPa were generated at the surface of rock mass (dotted circle, upper extreme right, Fig. 18b). These tensile stresses could cause vertical propagation of incipient fractures by thermal

fatigue near or at the surface of rock mass, thus destabilizing the rock mass. Small permanent fracture displacements (≈ 0.07 mm) are observed due to thermal stresses (difference in displacements between the end point (4) and start point (1)) as shown in Fig. 19a and b. Almost similar displacements were computed before and after correction (Fig. 19a and b) because A is very small (A = 0.002 mm/^{o}C).

For a more general discussion, the mechanism of closing and opening of fracture is briefly described. Fig. 20 depicts a steep fractured rock slope. As temperature increases (heating) fracture tends to close (Fig. 20a), this is because the outer strip (close to the cliff) is heated and it expands, resulting in fracture closure. As temperature decreases, fracture tends to open (Fig. 20b). This is because the outer rock mass and its vicinity contract, hence fracture opening.

Under the zero-crossing temperature (–2.2 ^{o}C), minor effects of freezing of pore water were observed (dotted circle, Fig. 21a and b). A small permanent fracture displacement (≈ 0.07 mm) was also observed (Fig. 21b).

8. Concluding remarks

To get better insight into the causative agents of rock falls, natural rock slope deformation across fractures in a chert rock mass was monitored using six surface fracture displacement sensors, and those arising from thermal stresses were predicted using two-dimensional finite element analysis. Using the new and simple proposed method (Eqs. (1) and (2)), the deformations can be divided into two parts: 1) those proportional to temperature variation, and 2) the other component u'(corrected displacement). The second component u' shows delayed and/or irrecoverable deformation in numerical analysis. By minimizing the first component (due to thermal response), the u' can be well recognized. After thermal correction of field data, under u', ch1 gave a clear rock mass movement, which could be related to fracture growth (see ch1, Fig. 8). Ch3 and 5, exhibit very small temperature-induced permanent fracture displacements (due to thermal change) over a period of over two years. Ch4 was gradually opening whilst ch6 was generally closing. Insignificant influences of weather conditions on fracture/rock mass movement were observed.

Our research also uncovered a couple of issues using numerical analyses. In the rock mass model (Fig. 9), tensile stresses that were large enough to induce fracture growth appeared at the fracture tip when temperature lowered. However, the small tensile stresses in the rock slope model (Fig. 17) would be sufficient to cause fracture growth along planes of weakness. It was also realised that fracture displacement was small (0.002 mm/^{o}C for 1m deep fracture), and that, for the rock slope model, non-linear deformations do not necessarily represent fracture propagation. Needless to mention, we appreciate that a three-dimensional model would be much realistic but due to the complex topography of the rock slope, a two-dimensional model was deemed appropriate.

After this investigation and analyses, what shall we say then? Our research suggests that the freezing effects on deformation of rock slope (predominantly in chert rock mass) are little or insignificant, and minor permanent fracture deformations occur under temperature variation across 0 ^{o}C (Figs. 8, 14d and 21b). We tentatively suggest that the permanent fracture deformations were dominantly caused by thermal fatigue. The yields from this study allow us to expand on our future investigations into the precursors leading to these rock falls. Though long-term segregation freezing and should be considered, we also acknowledge that there is a broad spectrum of damaging elements responsible for rock slope deformation and further monitoring would give valuable results.

References

Akagawa, S., Kodama, N., 2005. Frost weathering in rocks and mortar. Alaska Rocks, Proceedings of 40th U.S. Symposium on Rock Mechanics (USRMS), Anchorage,

Alaska, Paper number 05-759.

Alder, P.M., Thovert, J., 1999. Fractures and fracture networks. Kluwer Academic Publishers, Dordrecht, pp. 1–10.

Corkum, A.G., Martin, C.D., 2004. Analysis of a rock slide stabilized with a toe-berm: a case study in British Columbia, Canada. International Journal of Rock Mechanics and Mining Sciences, 41, pp. 1109–1121.

Crank, J., 1975. The mathematics of diffusion. Oxford university press, Oxford, pp. 144–146.

Davidson, G.P., Nye, J.F., 1985. A photoelastic study of ice pressure in rock cracks. Cold Regions Science and Technology 11, pp. 141–153.

Ishiguro, S., Nakaya, M., 1986. Temperature distribution analysis of concrete in fill dam gallery. Bulletin of the University of Osaka Prefecture, Ser. B, 38, pp. 35–43.

Ishikawa, M., Kurashige, Y., Hirakawa, K., 2004. Analysis of crack movements observed in an alpine bedrock cliff. Earth Surface Processes and Landforms 29, pp. 883–891.

Kostak, B., Dobrev, N., Zika, P., Ivanov, P., 1998. Joint monitoring on a rock face bearing an historical bas-relief. Quarterly Journal of Engineering Geology and Hydrogeology 31, pp. 37–45.

Martin, R.J. III, 1972. Time-dependent crack growth in quartz and its application to the creep of rocks. Journal of Geophysical Research 77, pp. 1406–1419.

Matsuoka, N., 2001. Direct observation of frost wedging in alpine bedrock. Earth Surface Processes and Landforms 26, pp. 601–614.

Matsuoka, N., 2008. Frost weathering and rockwall erosion in the southeastern Swiss Alps: long-term (1994–2006) observations. Geomorphology 99, pp. 353–368.

Murton, J.B., Peterson, R., Ozouf, J., 2006. Bedrock fracture by ice segregation in cold regions. Science, 314(5802), pp. 1127–1129.

Nicholson, D.T., Hencher, S.R., 1997. Assessing the potential for deterioration of engineered rockslopes, in: Marinos, P.G., Koukis, G.C., Tsiambaos, G.C., Stournaras, G.C. (Eds.), Engineering Geology and the Environment, Balkema, Rotterdam, pp. 911–917.

Nicholson, D.T., Lumsden, A.C., Hencher, S.R., 2000a. Excavation-induced deterioration of rockslopes, in: Landslides in research, theory and practice, London, Thomas Telford, vol. 3, pp. 1105–1110.

Nicholson, D.T., Nicholson, F.H., 2000b. Physical deterioration of sedimentary rocks subjected to experimental freeze-thaw weathering. Earth Surface Processes and Landforms 25, pp. 1295–1307.

Pantelidis, L., 2009. Rock stability assessment through rock mass classification systems. International Journal of Rock Mechanics and Mining Sciences, 46, pp. 315–325.

Reddy, J.N., 1993. An introduction to the finite element method. McGraw-Hill, 2nd edition, pp. 295–403.

Rose, N.D., Hungr, O., 2007. Forecasting potential rock slope failure in open pit mines using the inverse-velocity method. International Journal of Rock Mechanics and Mining Sciences, 44, pp. 308–320.

Saito, M., 1965. Forecasting the time of occurrence of a

slope failure. Proceedings of 6th International Conference on Soil Mechanics and Foundation Engineering, Montreal, 2, pp. 537–541.

Saito, M., 1969. Forecasting time of slope failure by tertiary creep. Proc. of 7th International Conference on Soil Mechanics and Foundation Engineering, Mexico City, 2, pp. 677–683.

Scholz, C.H., 1972. Static fatigue of quartz. Journal of Geophysical Research 77, pp. 2104–2114.

Shiotani, T., 2003. Evaluation of rock stability by means of acoustic emission. International Conference on Emerging Technologies in Non-Destructive Testing, Keynote lecture, Greece.

Stemberk, J., Kostak, B., Cacon, S., 2010. A tectonic pressure pulse and increased geodynamic activity recorded from the long-term monitoring of faults in Europe. Tectonophysics 487, pp. 1–12.

Waragai, T., 1998. Effects of Rock Surface Temperature on Exfoliation, Rock Varnish, and Lichens on a Boulder in the Hunza Valley, Karakoram Mountains, Pakistan. Arctic and Alpine Research, 30, pp. 184–192.

Timoshenko, S.P., Goodier, J.N., 1969. Theory of elasticity. McGraw-Hill, New York, 2nd edition.

William, H.P., Teukolsky, S.A., William, T.V., Brian, P.F., 2007. Numerical recipes, The art of scientific computing. Cambridge University Press, New York, pp. 1045–1052.

Zienkiewicz, O.C., Taylor, R.L., 2005a. The finite element method for solid and structural mechanics. Elsevier Butterworth-Hienemann, Oxford, 6th edition, pp. 3–16.

Zienkiewicz, O.C., Taylor, R.L., Zhu, J.N., 2005b. The finite element method: Its basis and fundamentals. Butterworth-Hienemann, Oxford, 6th edition, pp. 188–241.

Table 1
Properties of rock mass used in numerical model

Property	Symbol	Value	Formula
Young's modulus	E	110 (GPa) [m]	
Poisson's ratio	ν	0.2 [a]	
Uniaxial compressive strength	σ_c	181 (MPa) [m]	
Angle of internal friction	ϕ	30° [a]	
Friction angle of rupture plane	ϕ'	30° [a]	
Tensile strength (intact)	σ_t	20.4 (MPa) [m]	
Residual tensile strength	σ_t'	0 (MPa) [a]	
Thermal conductivity	K	7.40 (W/ m K) [m]	
Specific heat	c	995 (J/ kg K) [m]	
Density	ρ	2636 (kg/m^3) [m]	
Expansion coefficient	α	7.94×10^{-6} (K^{-1}) [a]	
Effective porosity	η	0.8% [m]	
Volumetric ice expansion due to freezing	ε_v	9% [a]	
Linear expansive strain due to freezing	ε_f	0.00036 [a]	$\sim(\eta \times \varepsilon_v)/2$*
Temperature at which freezing starts	T_1	0 °C [a]	
Temperature at which freezing finishes	T_2	–30 °C [a]	

[a] assumed; [m] measured; [*] 2 is used because of plane strain analysis.

Table 2
Maximum tensile stress results under elastic analysis

Temperature range	**Elastic analysis**	
	Boundary conditions	
	Confined	Unconfined
7.8–32.2 °C	30.8 MPa at 7.8 °C	13.2 MPa at 7.8 °C
–2.2–22.2 °C	29.2 MPa at –2.2 °C	12.4 MPa at –2.2 °C

Table 3
Tensile failure of elements under elasto-plastic analysis

Temperature range	**Elasto-plastic analysis**	
	Boundary conditions	
	Confined	Unconfined
7.8–32.2 °C	6 elements failed at 7.8 °C	0 (no element failure)
–2.2–22.2 °C	4 elements failed at –2.2 °C	0 (no element failure)

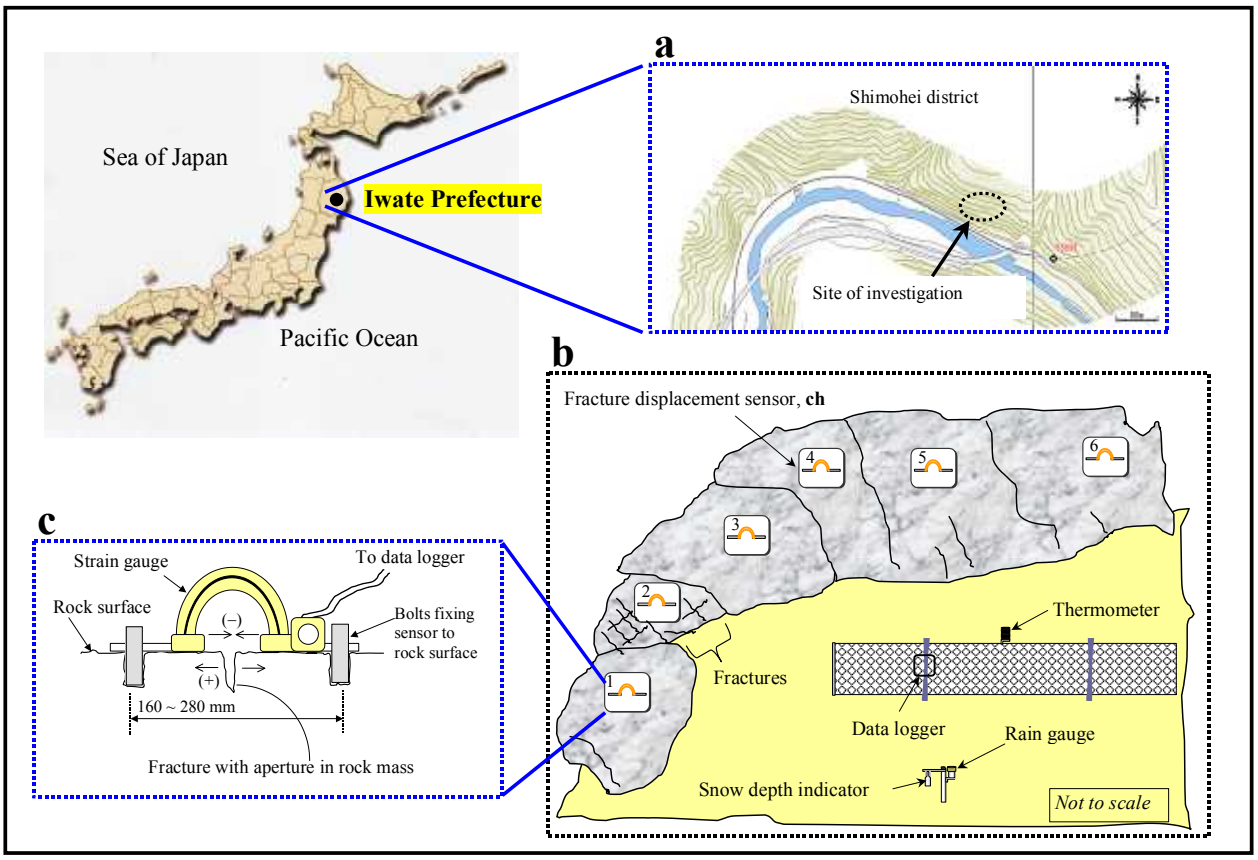

Fig. 1. (a) Topographic view for the investigation site, (b) Schematic diagram of natural rock slope showing layout of fracture displacement sensors and meteorological equipments, and (c) Setting of fracture displacement sensor.

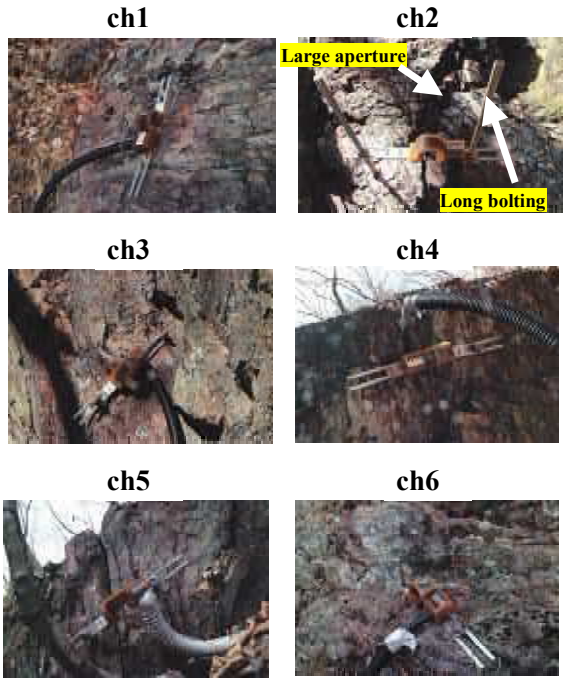

Fig. 2. Fracture displacement sensors (ch1–ch6) installed on surface of natural rock slope in Iwate prefecture (Japan).

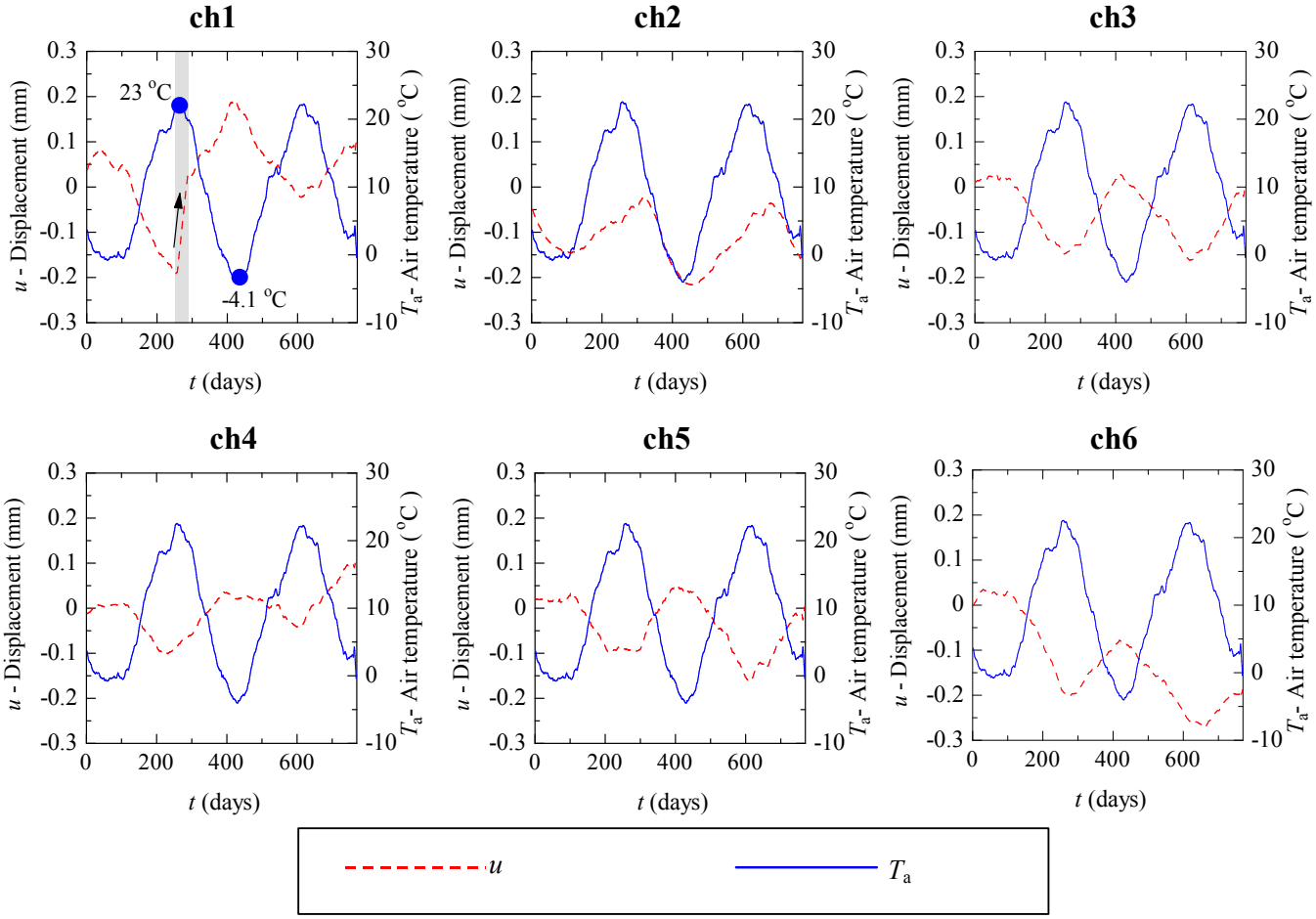

Fig. 3. Temporal variations in displacement u (daily average) and air temperature T_a (daily average) for six surface fracture displacement sensors, ch1–ch6. A sharp movement (arrow) occurred at t = 257–286 days.

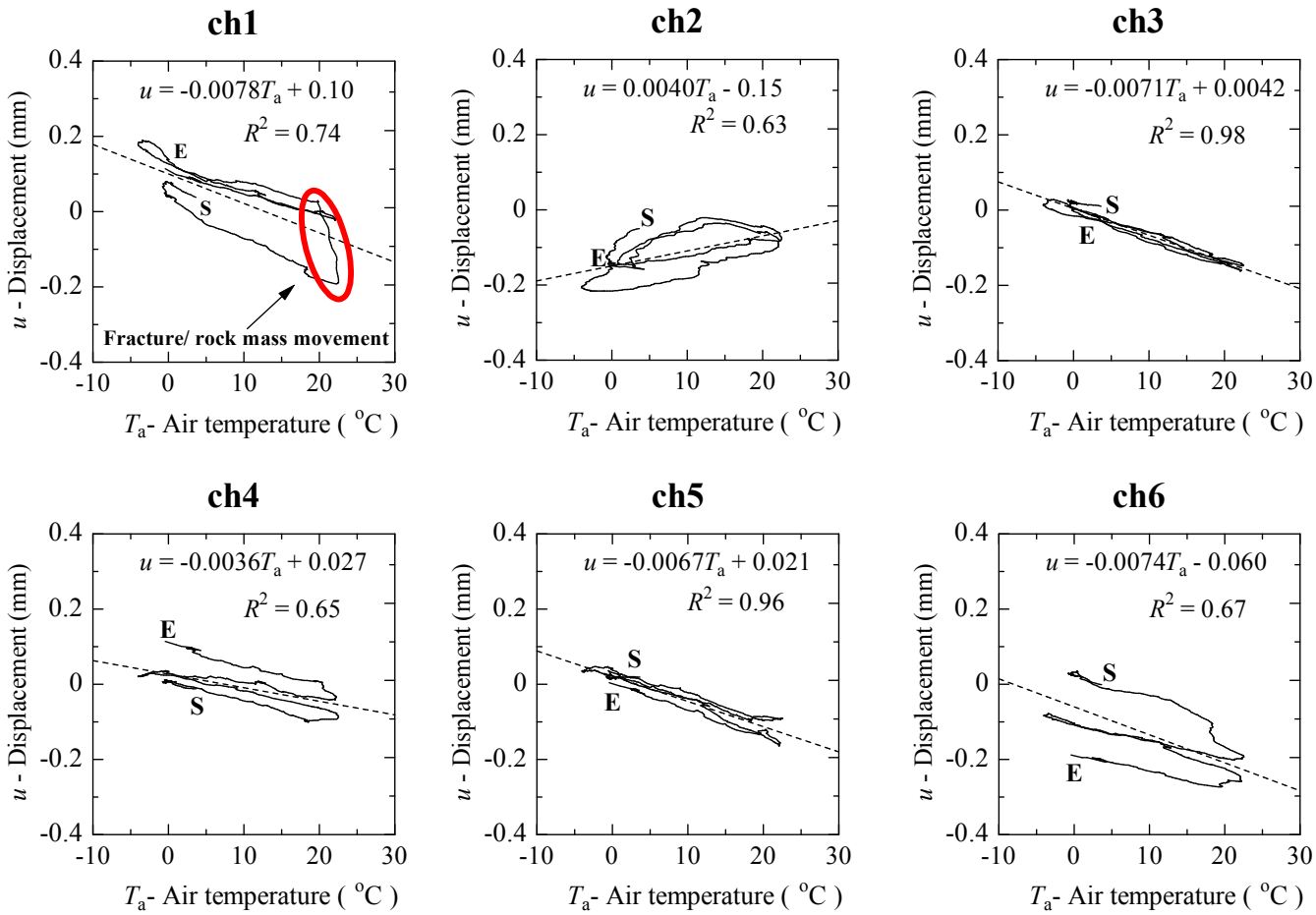

Fig. 4. Temporal variations in displacement u (daily average) against air temperature T_a (daily average) for ch1–ch6. *Note*: S and E denote the start and end of monitoring.

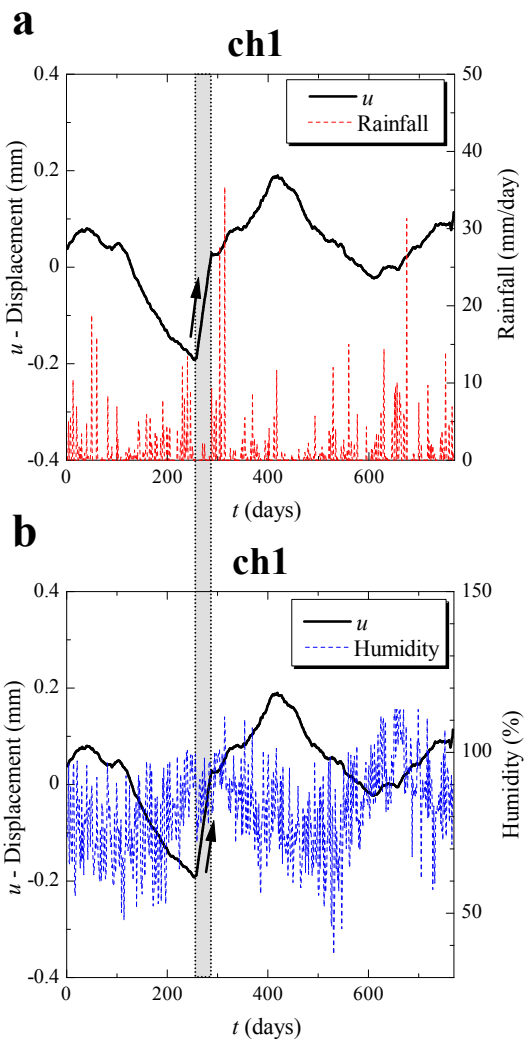

Fig. 5. Temporal variations in displacements and meteorological factors for ch1: (a) displacement vs. rainfall, (b) displacement vs. humidity. A sharp movement (arrow) occurred at t = 257–286 days.

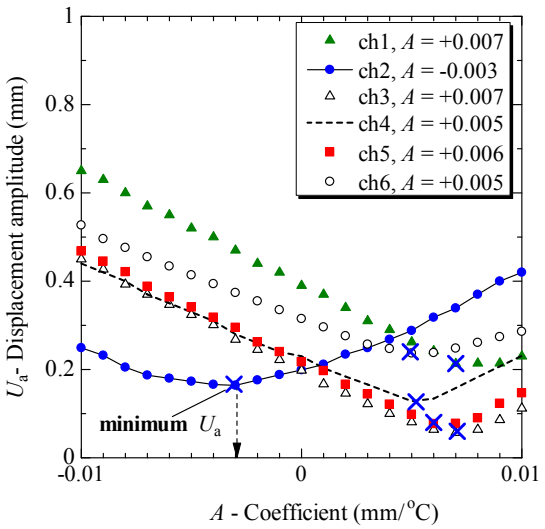

Fig. 6. Displacement amplitude U_a vs. thermal correction coefficient A, for six surface fracture displacement sensors, ch1–ch6. Symbol ×, depicts points of minimum temperature effects.

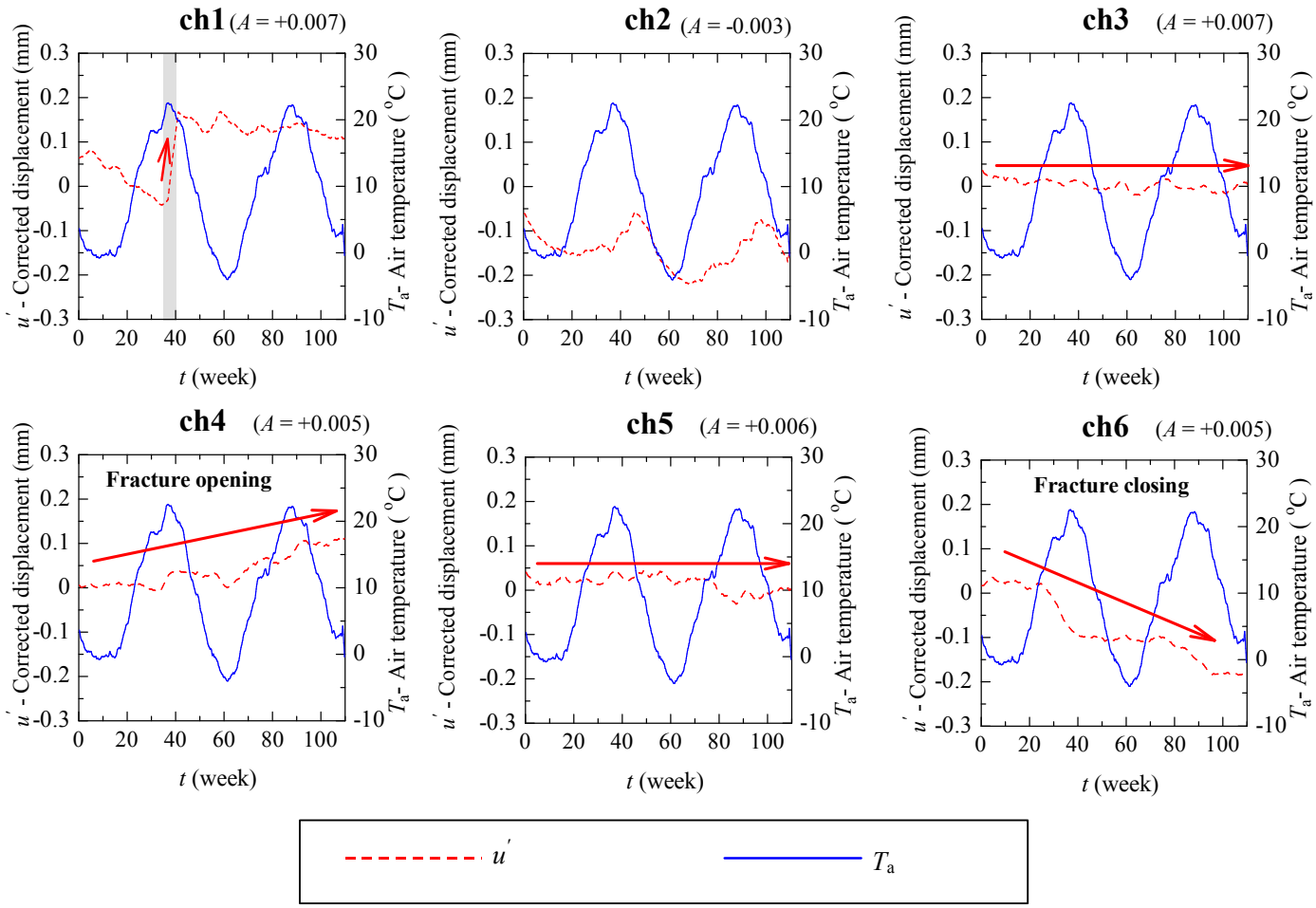

Fig. 7. Temporal variations in corrected displacement u' (moving averaged) and air temperature T_a (moving averaged) for ch1–ch6.

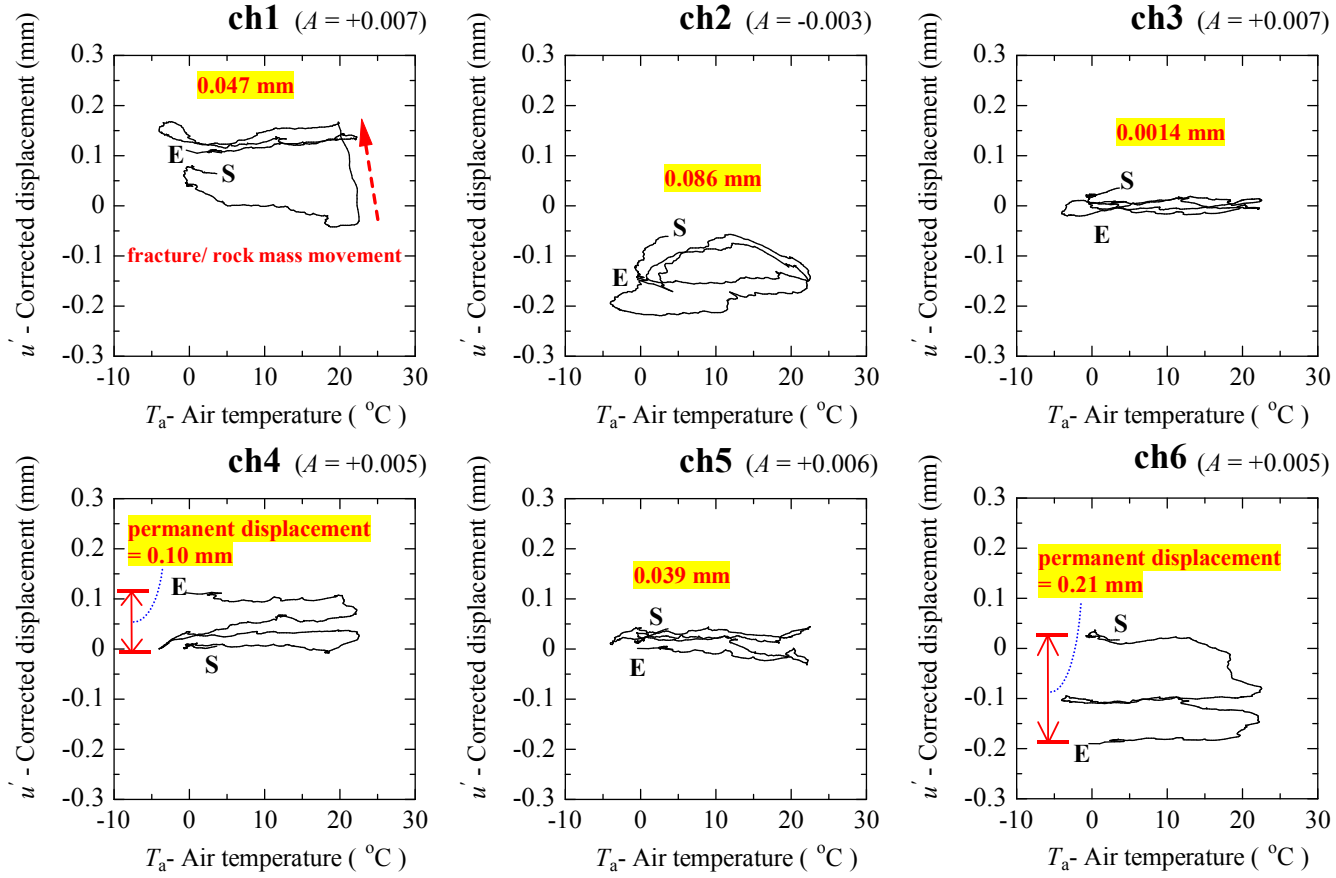

Fig. 8. Temporal variations in corrected displacement u' (daily average) and air temperature T_a (daily average) for ch1–ch6. *Note*: S and E denote the start and end of monitoring.

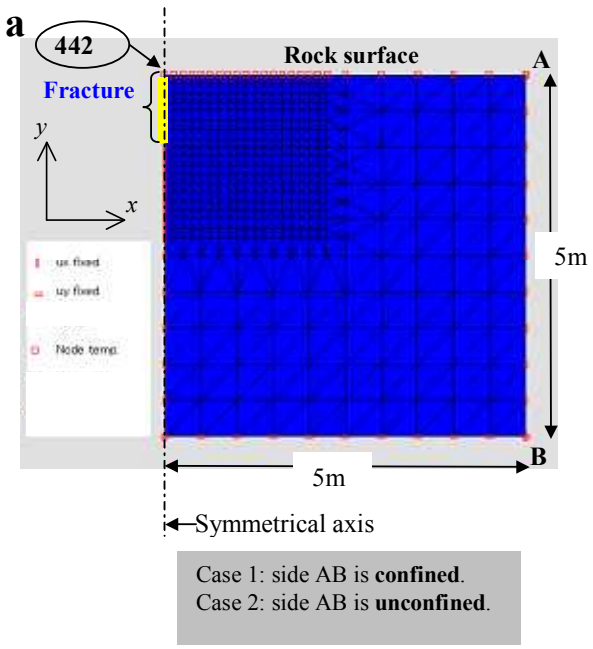

Fig. 9. Finite element mesh configuration used in numerical simulation for confined and unconfined boundary conditions: *Note*: 442 is node number that represents the beginning of the fracture at the rock surface. The fracture has some aperture.

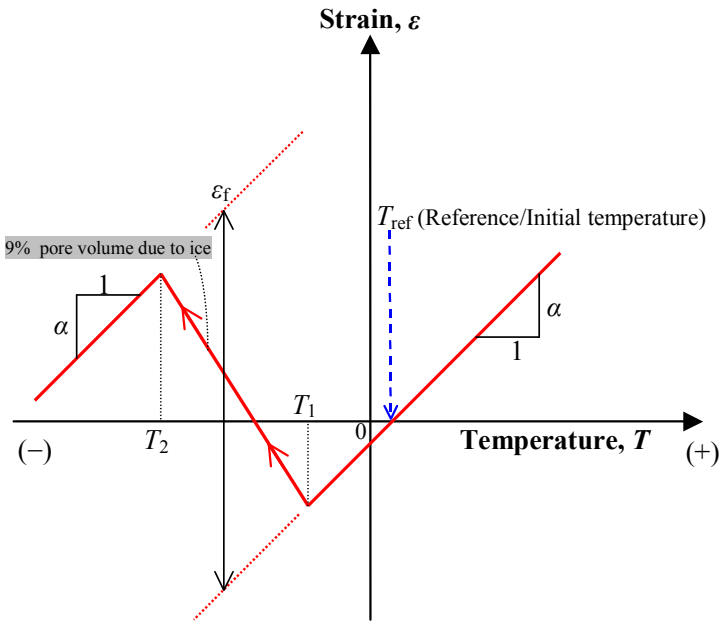

Fig. 10. Model for expansion due to freezing of pore water.

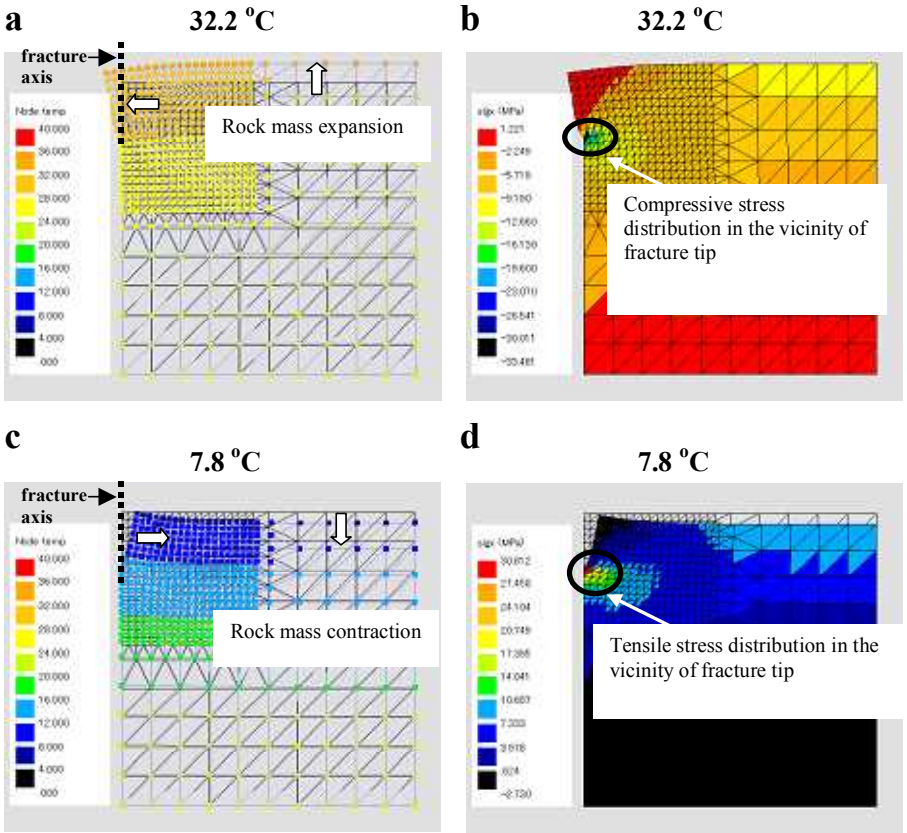

Fig. 11. Calculated results of Elastic-confined FE model: (a) Temperature distribution in rock mass at maximum temperature, 32.2 °C, (b) Stress in *x*-direction (sigx/σ_x) at 32.2 °C, (c) Temperature distribution in rock mass at minimum temperature, 7.8 °C, and (d) σ_x at 7.8 °C. *Note*: Deformation is magnified × 1000.

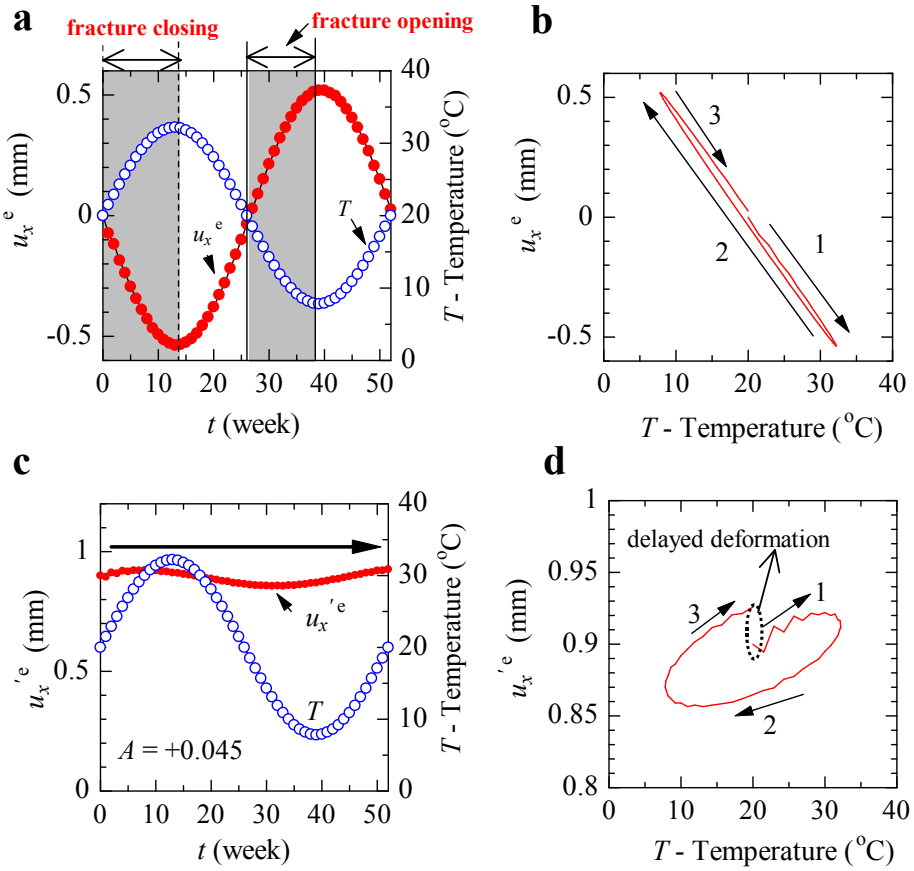

Fig. 12. Calculated results of Elastic-confined FE model: (a) Temporal variations in thermal displacement and temperature, (b) thermal displacement vs. temperature, (c) temporal variations in corrected thermal displacement and temperature, and (d) corrected thermal displacement vs. temperature. Thermal correction coefficient A = +0.045 mm/°C. Numbered arrows show sequence of opening and/or closing of fracture from the start (1) to the end (3) of analysis under temperature variations. Note: Positive displacements mean fracture opening and negative displacements mean fracture closure.

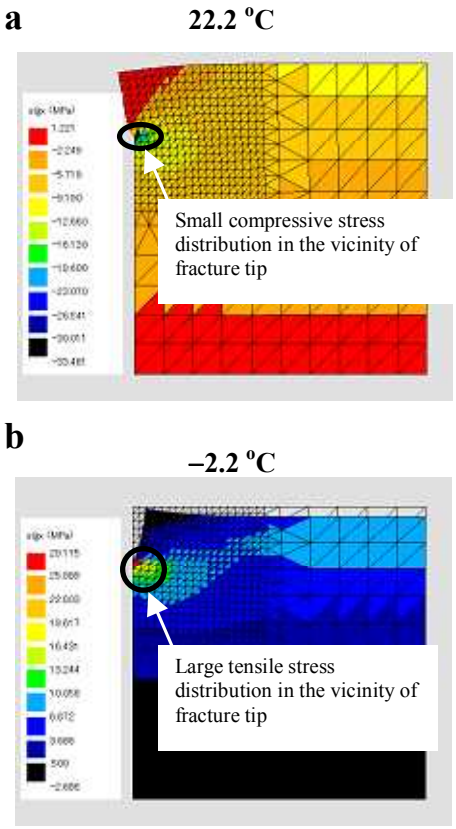

Fig. 13. Calculated results of Elastic-confined FE model: (a) Stress in *x*-direction (sigx/σ_x) at maximum temperature 22.2 °C and (b) sigx/σ_x at –2.2 °C. *Note*: Deformation is magnified × 1000.

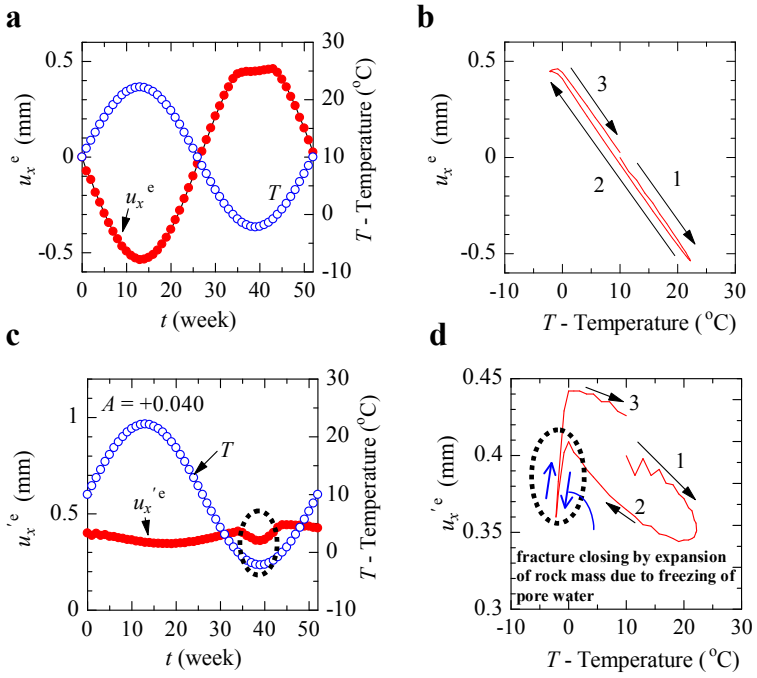

Fig. 14. Calculated results of Elastic-confined FE model: (a) Temporal variations in thermal displacement and temperature, (b) thermal displacement vs. temperature, (c) corrected thermal displacement vs. time, and (d) temporal variations in corrected thermal displacement and temperature. Thermal correction coefficient A = +0.040 mm/°C. Numbered arrows show sequence of opening and/or closing of fracture from the start (1) to the end (3) of analysis under temperature variations.

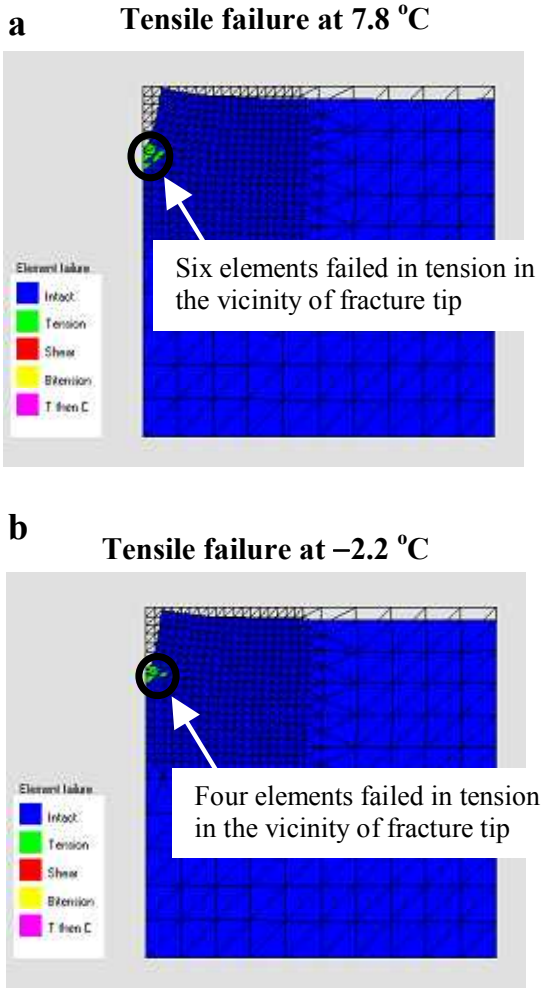

Fig. 15. Calculated results of Elasto-plastic confined FE model: (a) Element failure at minimum temperature 7.8 °C and (b) Element failure at minimum temperature –2.2 °C. *Note*: Deformation is magnified × 1000.

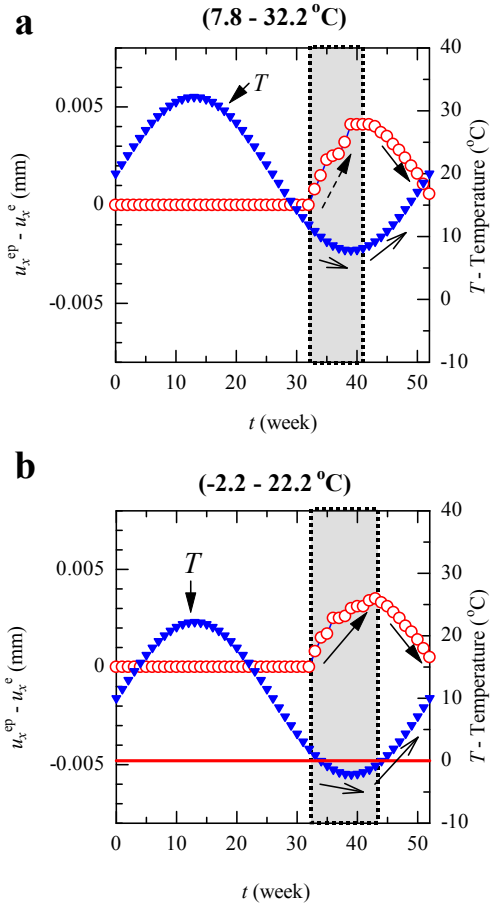

Fig. 16. Displacement in confined conditions at two temperature ranges: (a) 7.8–32.2 °C and (b) –2.2–22.2 °C.

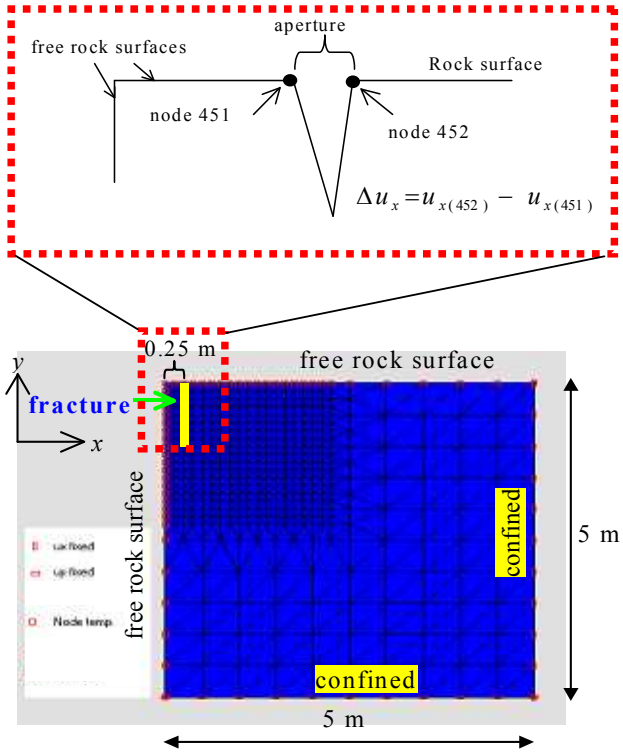

Fig. 17. Finite element mesh configuration used in numerical simulation under confined boundary conditions. The fracture has some aperture.

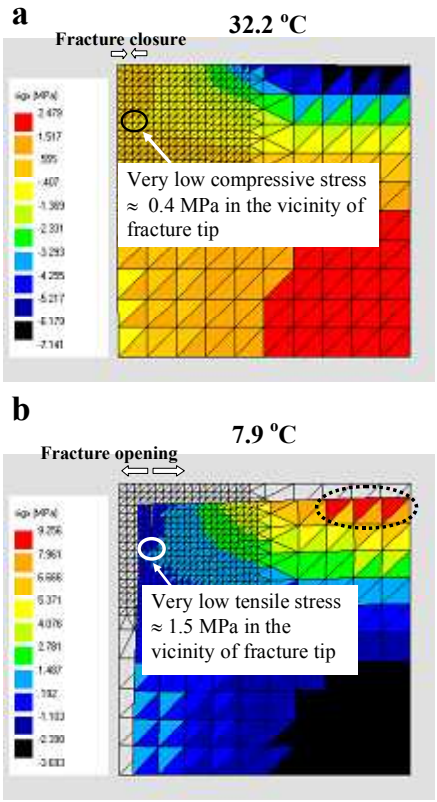

Fig. 18. Calculated results of Elastic FE model: (a) Stress in x-direction (sigx/σ_x) at 32.2 °C and (b) Stress in x-direction σ_x at 7.9 °C. *Note*: Deformation is magnified × 1000.

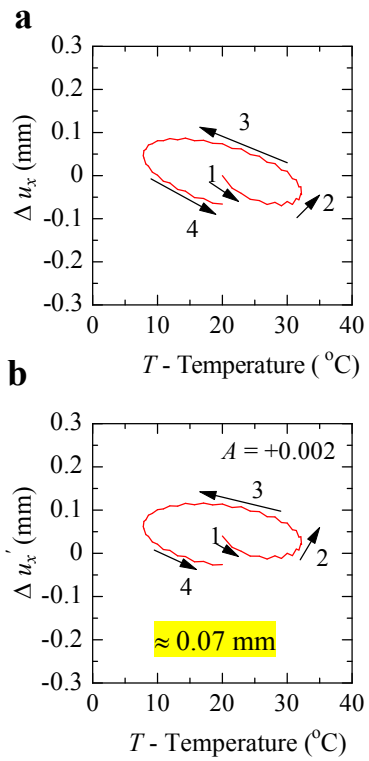

Fig. 19. Calculated results of Elastic FE model in the temperature range (7.8–32.2 °C): (a) thermal displacement vs. temperature, and (b) corrected thermal displacement vs. time. Thermal correction coefficient A = +0.002 mm/°C. Numbered arrows show sequence of opening and/or closing of fracture from the start (1) to the end (4) of analysis under temperature variations.

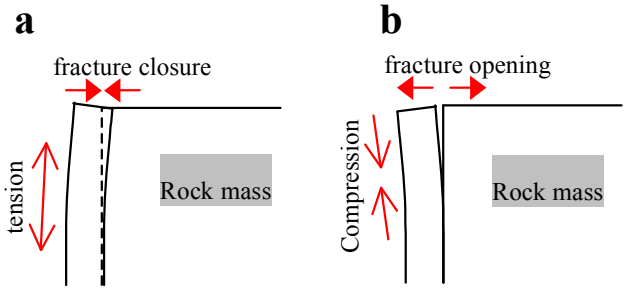

Fig. 20. Mechanism of fracture movement: (a) fracture closure under high temperatures and (b) fracture opening under low or sub-zero temperatures.

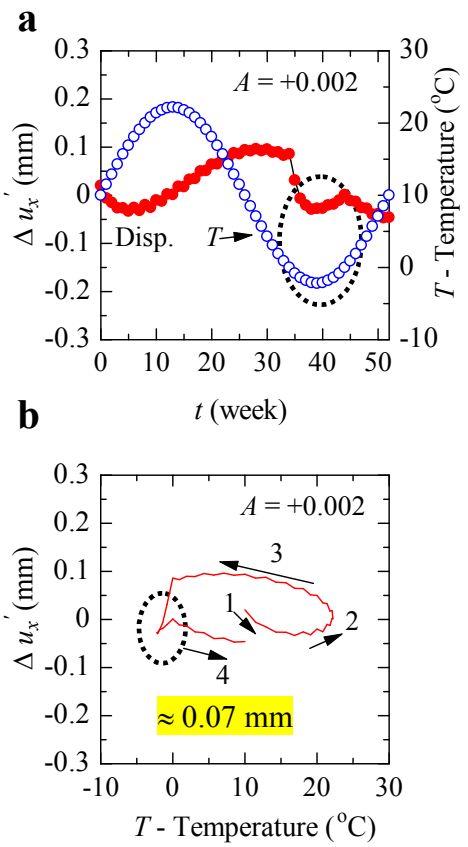

Fig. 21. Calculated results of Elastic FE model in the temperature range (–2.2–22.2 °C): (a) Temporal variations in corrected thermal displacement and temperature, and (b) corrected thermal displacement vs. temperature. Thermal correction coefficient A = +0.002 mm/°C. Numbered arrows show sequence of opening and/or closing of fracture from the start (1) to the end (4) of analysis under temperature variations. The encircled portions shows expansion due to freezing of pore water in the rock mass.